Engineering with Computers
https://doi.org/10.1007/s00366-024-02068-x

ORIGINAL ARTICLE

Concept for a geometry-insensitive high-field magnetic resonance detector

Khai Chau-Nguyen[1] · **Vlad Badilita**[1] · **Jan G. Korvink**[1]

Received: 12 June 2024 / Accepted: 25 September 2024
© The Author(s) 2024

Abstract

We introduce an inverse design methodology for a new class of eigenfrequency-invariant metamaterial-resonators, targeting nuclear magnetic resonance detection at ultra-high $\mathbf{B_0}$ field, and operating at two specified frequencies selected from within the 100-1500 MHz range. The primary optimisation goal is to maximise the magnetic field intensity and uniformity within a liquid sample, while the electric energy should be kept to a minimum level to reduce dielectric heating or quadrupolar moment excitation effects. Due to the symmetric geometry requirement of the cavity, a demultiplexer is also designed to direct each discrete resonant signal to another predetermined output port of the resonator. In order to reduce the geometrical dependency of the resonance frequency, a bespoke metamaterial is used for the cavity host. Therefore, an additional optimisation problem for a unit cell domain is defined to seek a proper material layout for the host region of the resonators. Given the sensitivity of the frequency domain, the optimisation process is effectively regulated through the utilisation of both a Helmholtz filter and a projection method. It is found that considerable improvements of the resonator quality factor can be obtained through this optimisation process.

Keywords Double-resonant resonators · Topology optimisation · Ultra-high field NMR · Metamaterials · Eigenfrequency-invariant detectors · Demultiplexer

1 Introduction

Faraday induction, through the invocation of the reciprocity principle [1], is one of the most widely used mechanisms to detect the time-varying nuclear magnetisation signal of a sample. The detector is usually an inductor, such as a coil or an electromagnetic waveguide. In order to achieve a stronger signal, the inductor is resonantly tuned by additional capacitance, allowing the power of the captured signal to propagate cyclically in phase with itself, as it dissipates in the electrical resistors of the circuit. For a conductor coil (a solenoid or spiral), tuning is typically achieved by adding lumped capacitance in parallel with the inductor (called an LC-resonator) so that the wave oscillates between the electrical and magnetic energy domains as it traverses the circuit. For a waveguide, the layout and hence effective dielectric constant of the waveguide are designed to produce a tuned resonator, with the wave reflecting from the ends as it propagates up and down the waveguide. The literature is replete with a large variety of nuclear magnetic resonance (NMR) detector coils such as the solenoid coil [2], Helmholtz coil [3], scroll coil [4], standing micro coil [5], cone-shaped gradient coil [6], cylinder spiral coil [7], micro planar coil [8], birdcage RF coil [9] and waveguide arrangements [10–12] that are suitable for detecting magnetic resonance signals. The evaluation of radiofrequency (RF) coils, concerning signal-to-noise ratio (SNR) and the homogeneity of magnetic resonance images, was recently conducted in the context of ultrahigh-frequency (UHF) 7T magnetic resonance imaging (MRI) [13]. Consideration was also given to the progress in NMR probes and microcoil development, specifically intended for miniaturised systems employed in the analysis of tiny samples [14]. Recently, a high-density coil array

---

✉ Jan G. Korvink
jan.korvink@kit.edu

Khai Chau-Nguyen
khai.chau@kit.edu

Vlad Badilita
vlad.badilita@kit.edu

[1] Institute of Microstructure Technology, Karlsruhe Institute of Technology (KIT), Hermann-von-Helmholtz-Platz 1, Eggenstein-Leopoldshafen 76344, Baden-Württemberg, Germany

Published online: 19 November 2024

has been designed and tested to satisfy the requirement of a higher SNR and high-resolution functional imaging [15]. For the purpose of improving the field homogeneity in the 9.4 T system, a superconducting shim coil design was acquired by a numerical optimisation method [16]. A given resonant tuning of coil and waveguide detectors must be adapted when the electrostatic or magnetostatic properties of the sample change significantly, since then the electromagnetic wave propagation speed inside the resonator will change, which will affect the match of the resonance frequency of the NMR signal and the resonator. The same is true for any changes in the shape of the detector; for then, the effective permeability and/or permittivity of the resonator will also experience a change, again affecting the resultant resonant frequency.

It is also possible to produce a resonant electromagnetic structure using a cavity, often benefiting from a better quality factor than a waveguide or an LC-resonator, by avoiding lossy materials and hence achieving a stronger net signal amplification. Because the vacuum electromagnetic wavelength of typical nuclear magnetic resonance signals is in the range of 10 cm to a metre (corresponding to the ^{1}H Larmor frequency from 300 MHz at 7T to 3 GHz at 70T), pure cavities have not played an important role in the detection of NMR. For electron spin resonance, with frequencies in the 10–100 GHz regime, wavelengths are much shorter, and hence cavities are more commonly used [10, 17–19].

The analytical treatment of the singular electromagnetic response triggered by near-zero index (NZI) or epsilon-near-zero (ENZ) materials is a highly interesting topic for optical applications. NZI media have been demonstrated to exhibit a variety of exciting and occasionally surprising optical effects since groundbreaking works were conducted in direct emission [20], band gaps in the visible wavelength range [21], propagation and scattering [22], electromagnetic energy tunnelling [23], supercoupling [24–26], emission control [20, 22, 27], photon tunnelling [28–30], and optical non-linearity [31–33]. In these applications, the space-time decoupling effect is usually activated due to the stretched wavelength of the electromagnetic signal during transmission in this extreme medium. The resonant frequency is thus determined by the dispersion of the material, in particular, the frequency at which the ENZ property is achieved, rather than the shape. Recent developments in ENZ metamaterials have opened up new possibilities in optics, photonics, and materials science. These materials are characterised by a dielectric permittivity near zero at certain frequencies, enabling unique electromagnetic properties like near-infinite phase velocity and enhanced wave-matter interactions. Li et al. demonstrated the ability to invert optical nonlinearity in ENZ materials, an exploration that could lead to highly efficient all-optical switches for photonic circuits [34]. In the field of advanced material fabrication, biocompatible ENZ materials were developed using silver nanoparticles in a polystyrene matrix, achieving a broadband response in the radio-frequency range (10 kHz–1 MHz) [35]. Another ENZ response in the sub-GHz range was also achieved using a new class of ternary metacomposites [36]. In 2016, Liberal et al. [37] postulated the existence of geometry-invariant resonant cavities induced by ENZ media, that is, whose eigenfrequencies are invariant to volume-conserving morphing of their shape. We hereby introduce this concept in the realm of magnetic resonance detection and we expect this to lead to a breakthrough in the development of high-quality magnetic resonance detection probes.

Topology optimisation is a highly effective computational design technique that has gained widespread application in multiphysics [38–42], including electromagnetics and photonics [43–46]. This approach involves optimising the layout or distribution of materials within a given design space to meet specific performance criteria, while satisfying constraints such as the total volume or cost. It has been utilised in the design of numerous electromagnetic devices, including antennas [47, 48], waveguides [49, 50], and metamaterials [51–54], among others [55–57]. The benefit of topology optimisation has been shown to significantly improve device performance, resulting in higher efficiency, reduced weight, and improved bandwidth. It has proven especially useful in the design of cavity resonators, where the optimal material distribution within the resonator structure can be sought to achieve desired resonant frequencies and other performance criteria [58–61]. This approach has been shown to improve the performance of cavity resonators, leading to more efficient and precise excitation and detection of signals. One of the primary advantages of topology optimisation in cavity resonator design is that it allows the development of more complex and intricate resonator geometries that would be challenging to design using conventional methods. Topology optimisation has been particularly auspicious in the design of surface plasmon resonances (SPPs) [62, 63], optical cloak [64], dielectric resonator [60], and non-conventional cavity resonators, such as dualmode and broadband resonators [65].

Surface plasmon polaritons (SPPs) [62, 63, 66, 67] are usually observed as the trapped electromagnetic waves that propagate along a dielectric-metal interface, where the real part of the permittivity turns its sign from negative to positive. These phenomena are originally perceived at optical wavelengths because of the interaction between light and nanoscale conductive surfaces [68–70]. In this range, the wavelength matches well with the feature sizes of structures that support SPPs. The conditions for observing SPPs become challenging in the radio frequency (RF) range which is defined for longer wavelengths. The RF electromagnetic waves are typically attenuated in interaction with metal surfaces, which does not support the formation of traditional SPPs, as observed in the optical regime. However, it is important to know if there are similar interactions that exhibit plasmonic-like behaviour in the RF range. These phenomena have been acknowledged in extremely high RF frequencies with applications for phase modulators [71] and antennas [72, 73]. Basically, SPPs-like waves can be supported by the combined effects of the metal-dielectric interface and the electromagnetic properties of the medium. When an interface is formed between an SPP material and another material, it can give rise to unique electromagnetic phenomena, including the excitation and manipulation of ENZ. The low permittivity of the SPPs material alters the dispersion properties of the ENZ, leading to interesting effects. For example, several instruments have been employed to excite a so-called spoof SPPs mode such as a waveguide and frequency splitter [74], microstrips [75], and a slot line [76] in microwave engineering. Here, we introduce a new approach to design the epsilon-near-zero (ENZ) metamaterial based on the spoof plasmonic behaviour within the RF range. The equivalent properties of this artificial zero index medium depend not only on the proportion of opposite-sign-permittivity materials but also on the mixture's topology. Furthermore, the frequency-dependent nature of SPPs is also relieved through an optimisation process, ensuring the validity of ENZ cells in double-resonant operation.

In this contribution, we build upon the concept of a new generation of resonators induced by epsilon-near-zero materials, towards a design that facilitates the high-efficiency nuclear magnetic resonance detection in a cavity, and overcomes some of the limitations resulting from the tuning sensitivity of conventional detectors to variations in sample properties and geometry:

- **Shape and loading invariance of the cavity resonance frequencies.** The primary nonideality of coil or transmission line detectors is their sensitivity to dielectric loading. The present ENZ-hosted cavity-based design is making a breakthrough by inherently overcoming this limitation.
- **Multiple ports, with resonances located in the sample volume.** The cavity features sample-centred mode shapes, i.e., with their magnetic field maxima stretching over the sample region, and the electric field maxima trapped outside of the sample region to avoid dielectric losses and coupling to the quadrupolar moments of the sample.
- **Port isolation.** In reception mode, the signal leaves the cavity from a selected port and is selectively blocked from transmission through the other port. The frequencies must be selectable by design (in this paper chosen and demonstrated for ^{13}C and ^{1}H), and thus feature good frequency isolation among the ports.
- **High quality factor.** The cavity should feature low internal loss mechanisms, with $Q > 1000$.
- **Realisability.** The resulting design must be manufacturable.

2 Concept and methodology

2.1 Concept of a distributed NMR resonator

A conventional LC resonator is shown in Fig. 1**a** as a typical detector used in most current NMR systems. In any circuit of lumped elements, the resistive loss in the inductor is a

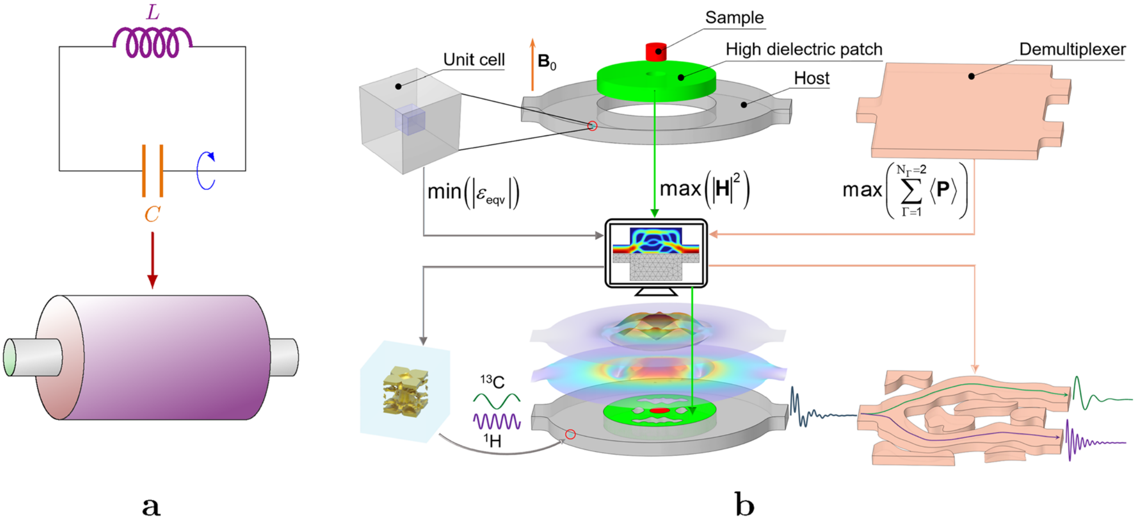

Fig. 1 **a** A transition from a conventional lumped LC circuit to a cavity resonator, which spatially distributes inductance and capacitance. **b** The eigenfrequency-invariant detector system is introduced as a combination of three topology optimisation problems: the ENZ metamaterial at the scale of a local unit cell, the magnetic double-resonant cavity at the sample location, and the demultiplexer

primary loss that increases with lower skin depth at higher frequencies. By translating the LC circuit, which is made from lumped elements, into a three-dimensional structure, we obtain an equivalent resonant cavity with decreased inductance. The loss in a cavity is mainly caused by the conducting wall, which can be reduced by using a smooth high-conductivity material. It is therefore necessary to develop a cavity-based multimode resonator that dominates the LC resonator in terms of efficiency and stability.

Highlighting the application of our universal optimisation method, we exemplify its implementation in the construction of a tailor-made cavity NMR detector design at $B_0 = 28.2$ T. The Larmor frequency of typical nuclei (^{1}H, ^{3}He, ^{7}Li, ^{13}C, ^{15}N, ^{17}O, ^{23}Na, ^{31}P, ^{129}Xe) ranges from 122 MHz to 1.2 GHz at this field strength. Among these isotopes, the ^{13}C and ^{1}H nuclei are important in NMR because these nuclei are abundant in organic molecules, their NMR signals provide detailed information about molecular structures, and their sensitivity allows for the analysis of a wide range of samples. Therefore, the resonator is built for these two candidates, aligning the resonant frequencies of 300 MHz and 1.2 GHz. The corresponding wavelengths of this specific and spectroscopically important frequency pair are 1 m and 0.25 m, respectively. Figure 1**b** presents the conceptual schematic of the geometry-invariant double resonant cavity design. At the top, the computational domains and their corresponding objective functions are shown: on the left, the smaller cube inside the cell is used as the designable area which is tailored to minimise the absolute equivalent permittivity; in the middle, an exploded view of the cavity shows the green coloured high dielectric patch which is considered to change its topology to maximise the magnetic intensity in the red coloured sample; and on the right, the design region is also the computational domain which is optimised to transmit the most proportion of the power flow in each frequency to the corresponding port. In the center, the numerical method-based optimiser is utilised to deal with the design tasks. At the bottom, the illustration highlights the achievements and behaviors: on the left, the final dopant is marked in gold; in the middle, the resonator is excited on the input port at both ^{1}H and ^{13}C frequencies to obtain the double resonance (with overlapped B_1 fields in the sample) and collect NMR combined signal on the output port; and on the right, the optimised demultiplexer receives the signal from the cavity and splits it into two distinct FID curves for analysis. Conventional design approaches have considerable difficulty in tackling this task, as optimised designs must demonstrate proficiency in operating within a double-resonant regime. This obstacle can be mitigated through the combination of a seamlessly integrated inverse design process with finite element solvers. The design problem is broken up into three topology optimisation problems, i.e., for the unit cell of the ENZ host material, for the high-dielectric material forming the cavity that accommodates the sample, and for the demultiplexer that serves to separate the two frequencies. In the first instance, the host microstructure is configured to attain an effective permittivity close to zero at both specified frequencies. Besides, the sample (red coloured region in Fig. 1**b**) is fully contained within the high dielectric patch whose topology must be optimised to localise the magnetic field maxima for each resonance mode within the sample region and orientated perpendicular to the static $\mathbf{B}_0$ field, and at the same time to separate the maxima of the electric field component so that these do not overlap with the sample. The magnetic field intensity should be homogeneous over the sample space, so that the position-dependent observation of the NMR signal is only influenced by the spin density. The third topology optimisation problem concerns the design of the demultiplexer that is connected to the output port of the cavity to separate the two frequencies. The formulation of each topology optimisation problem is presented in detail in the upcoming sections.

2.2 Governing equations

The relationships of the electric field, $\mathbf{E}$, and magnetic fields, $\mathbf{H}$, can be described using Maxwell's equations [77] throughout the modeling domain $\Omega = \{\Omega_I \cup \Gamma\}$ in $\mathbb{R}^3$, with the interior region Ω_I and the boundary Γ:

$$\begin{aligned}
\nabla \cdot \mathbf{E} &= \frac{\zeta}{\varepsilon_r \varepsilon_0}, \\
\nabla \cdot \mathbf{H} &= 0, \\
\nabla \times \mathbf{E} &= -\mu_0 \frac{\partial \mathbf{H}}{\partial t}, \\
\nabla \times \mathbf{H} &= \mathbf{J} + \varepsilon_r \varepsilon_0 \frac{\partial \mathbf{E}}{\partial t},
\end{aligned} \tag{1}$$

where ζ and $\mathbf{J}$ denote the charge density and current density, and t denotes time. Further, μ_0, ε_0, and ε_r are the vacuum permeability, the vacuum permittivity, and the relative permittivity of the medium, respectively. If there is no charge and current in the medium, the following equations are derived:

$$\mathcal{L}_{EM} = \begin{cases} \nabla \times \nabla \times \mathbf{E} - \omega^2 \mu_0 \varepsilon_0 \varepsilon_r \mathbf{E} & = \mathbf{0}, \\ \nabla \times \left(\dfrac{1}{\varepsilon_r} \nabla \times \mathbf{H} \right) - \omega^2 \mu_0 \varepsilon_0 \mathbf{H} & = \mathbf{0}, \end{cases} \tag{2}$$

where ω is the angular frequency, and $\mathcal{L}_{EM}$ is the differential operator acting on the electromagnetic field. The step of solving Maxwell's equations involves identifying the specific problem context, imposing boundary conditions on Γ, and using numerical methods in most complex/general cases.

2.3 Inverse design

For the topology optimisation procedure, we discretise the well-known Maxwell equations with the finite element method, as shown briefly in the Governing equations subsection with an assumption of time-harmonic field behaviour. The density-based method [38, 39] is employed to describe the material interpolation in the design regions. The *max*–type formulations were solved to enhance the power flow at each output port of the splitter, and the local magnetic field in the sample, whereas a *min*–type problem was implemented to find the microstructure of the ENZ material. We designed the variable-optimisation spaces to make the devices compatible with the RF wavelength of currently available NMR magnets. The optimisation procedure is carried out to update the design variables using the given material interpolation rule. During this process, the appearance of numerical issues such as spatial single-cell variations and the weak sense of length scale may cause slow convergence and instability to the optimiser. This barrier can be alleviated by applying the well-known Helmholtz PDE filter in the design region with homogeneous Neumann boundary conditions as

$$\begin{cases} \tilde{\rho}(\mathbf{x}) = \rho(\mathbf{x}) + r_{\min}^2 \nabla^2 \tilde{\rho}(\mathbf{x}), \text{ in } \Omega_D \\ \mathbf{n} \cdot \nabla \tilde{\rho}(\mathbf{x}) = 0, \text{ on } \partial\Omega_D, \end{cases} \tag{3}$$

where $r_{\min}$ is the desired filter radius, and $\rho(\mathbf{x})$ and $\tilde{\rho}(\mathbf{x})$ are the original and filtered design fields, respectively. Next, the smoothed Heaviside projection scheme is employed to improve the physical meaning of the filtered design variables,

$$\bar{\tilde{\rho}}(\mathbf{x}) = \frac{\tanh(\beta \cdot \eta) + \tanh(\beta \cdot (\tilde{\rho} - \eta))}{\tanh(\beta \cdot \eta) + \tanh(\beta \cdot (1 - \eta))}, \tag{4}$$

where $\beta \in [1, \infty]$ and $\eta \in [0, 1]$ are parameters used to control the threshold sharpness and value, respectively. Thus, the filtered design variables were transferred to the FE model by linear approximations. For symmetric constraints in optimisation, we chose user-defined mirror operators to ensure symmetry. With a focus on ensuring convergence of the solution in double resonance, we added volume fraction constraints $v_f = 50\%$ and $v_f = 80\%$ to the first and second problems, respectively. The numerical simulations in this paper were performed using COMSOL Multiphysics® 6.0 on a computer with an AMD Ryzen Threadripper 3970X and 256 GB of RAM. The PARDISO solver was selected to treat the linear systems derived from FEM because of its excellent performance, robust numerical stability, versatile matrix support, and scalability for handling very large problems [78]. All optimisation problems were solved using the integrated method of moving asymptotes (MMA) [79].

3 Numerical results

3.1 Zero index metamaterial

It is worth noting that the design and realisation of ENZ materials in the RF range are more challenging than those in the optical regime due to the longer wavelengths involved. The plasmonic [53] and ENZ effects can be realised by arranging materials in repeating patterns at a scale smaller than the working wavelengths. To obtain a solution for the sensible material distribution of the microstructure for the host, the topology optimisation method is illustrated in a unit cell as described in Fig. 2**a**. The unit cell is a cube with dimensions of 1 x 1 x 1 mm including the cubic designable domain Ω_D ($0.5 \times 0.5 \times 0.5$ mm). The boundary condition $\hat{\mathbf{n}} \times \mathbf{E} = 0$ is applied on Γ_E to enforce periodicity. Assuming that the incident field $\mathbf{E}_0$ propagates perpendicularly to Γ_1 and Γ_2, the first-order scattering boundary conditions imposed on these boundaries are

$$\begin{aligned} &\mathbf{n} \times (\nabla \times \mathbf{E}) - \mathrm{i}k_0 \mathbf{n} \times (\mathbf{E} \times \mathbf{n}) = -2\mathrm{i}k_0 \mathbf{E}_0 \text{ on } \Gamma_1, \\ &\mathbf{n} \times (\nabla \times \mathbf{E}) - \mathrm{i}k_0 \mathbf{n} \times (\mathbf{E} \times \mathbf{n}) = 0 \text{ on } \Gamma_2, \end{aligned} \tag{5}$$

where i is the complex unit, Γ_E denotes the lateral periodic boundaries, and Γ_1 and Γ_2 are the input and output boundaries, respectively. The design field $\rho(\mathbf{x})$ is introduced to describe the material distribution in the computational space Ω by the interpolation

$$\varepsilon(\rho) = \varepsilon_s + \rho\left(1 - \frac{{\omega_p}^2}{\omega^2 + \mathrm{i}\omega f_D} - \varepsilon_s(1 + \mathrm{i})\right), \tag{6}$$

where $\rho(\mathbf{x})$ denotes the material distribution of the high-κ dielectric in the design space, $\varepsilon(\rho)$ is the material interpolation of the permittivity used in topology optimisation problem, ε_s denotes the permittivity of the substrate (polyethylene/cross-linked polyethylene (XLPE)), and ω_p, ω, and f_D are the plasma frequency, design frequency, and damping constant of copper calcium titanate $CaCu_3Ti_4O_{12}$ (CCTO)/18 wt% multiwall carbon nanotube (MWCNT) negative index material [80], respectively. The average electric displacement $\langle \mathbf{D} \rangle_\Omega = |\Omega|^{-1} \int_\Omega \varepsilon(\rho)\mathbf{E}\mathrm{d}\Omega$ and the electric field $\langle \mathbf{E} \rangle_\Omega = |\Omega|^{-1} \int_\Omega \mathbf{E}\mathrm{d}\Omega$ are obtained by integrating the electric distribution over the computational domain. Then, the constrained continuous optimisation problem is constructed as

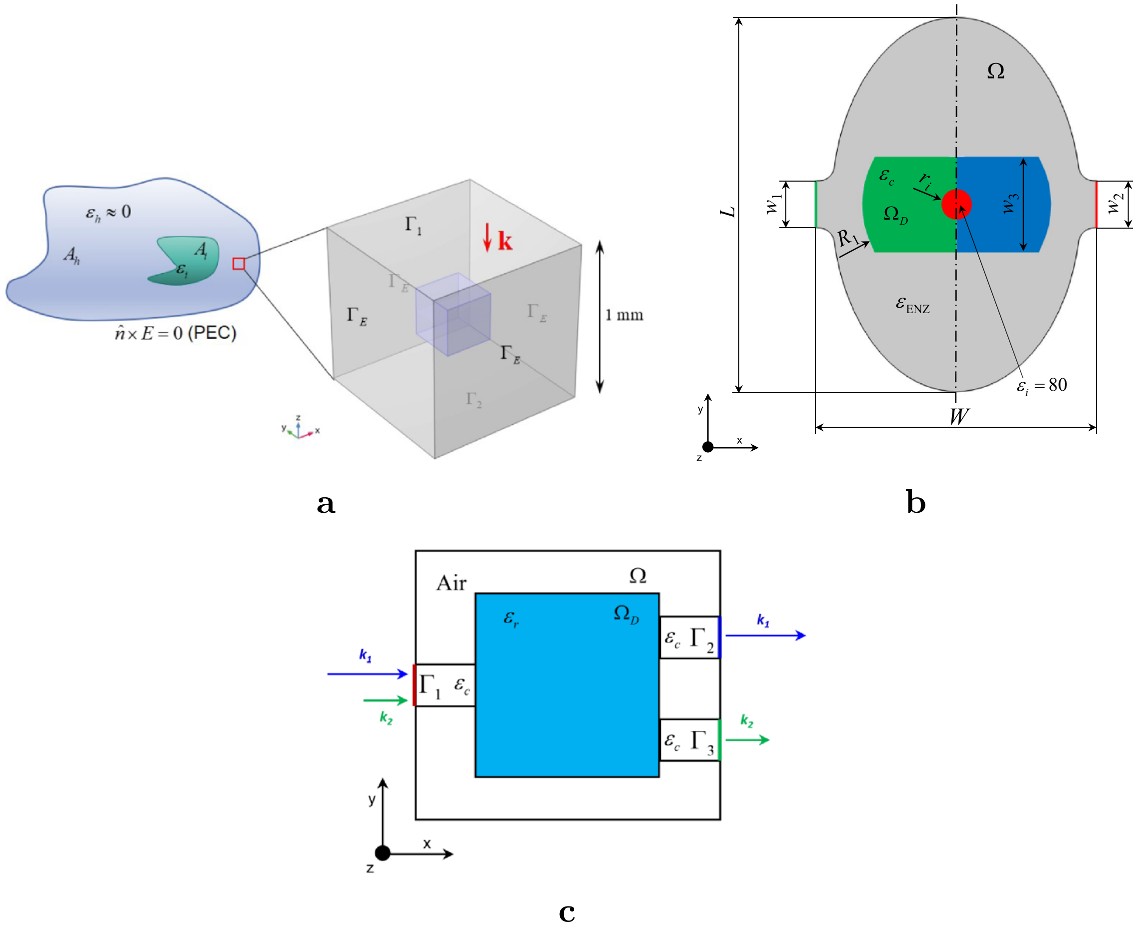

Fig. 2 **a** A representative cell domain for ENZ metamaterial design. **b** Sketch of the computational domain for the inverse design of the oval resonator cavity. **c** RF splitter domain for optimisation problem

$$
\begin{aligned}
&\min_{\rho(\mathbf{x})}\ \varepsilon_{\mathrm{eff}}(\rho) = \frac{\langle \mathbf{D} \rangle_{\Omega}}{\langle \mathbf{E} \rangle_{\Omega}},\\
&\text{s.t. } \mathcal{L}_{EM}(\mathbf{E}(\mathbf{x}), \rho(\mathbf{x})) = f(\mathbf{x}),\\
&\quad \varepsilon(\rho) = \varepsilon_s + \rho\left(1 - \frac{{\omega_p}^2}{\omega^2 + \mathrm{i}\omega f_D} - \varepsilon_s(1+\mathrm{i})\right),\\
&\quad 0 \le \rho_e \le 1, e = 1, 2, \ldots, \aleph_D,\\
&\quad \rho = 0 \forall \mathbf{x} \in \Omega \setminus \Omega_D.
\end{aligned}
\tag{7}
$$

Six symmetric constraints are included in the optimisation to ensure the validity of the design under an incident field from an arbitrary direction. Specifically, a set of planes used in the mirror operation is defined in three-dimensional space as $\mathcal{P} = \{P_1, P_2, P_3, P_4, P_5, P_6\}$, where each plane P_i is described by the following equations: $P_1{:}x = 0, P_2{:}y = 0, P_3{:}z = 0, P_4{:}z - y = 0, P_5{:}z + y = 0, P_6{:}z - x = 0$. The inner cubic design domain Ω_D is immersed in the unit substrate medium Ω. Essentially, the goal is to minimise the real part of the equivalent permittivity close to zero with an incident wave combined from two signals at the design frequency pair $f_1 = 300$ MHz and $f_2 = 1.2$ GHz ($\lambda_1 = 1$ m and $\lambda_2 = 0.25$ m). As a means to diminish the acummulative error of the numerical solutions, the designable domain is discretised into 17,576 cubic elements (26 segments per edge) while the outer substrate contains 102,360 tetrahedra and 4,350 pyramids. In the setup for optimisation, the optimality tolerance (in the MMA solver), the relative tolerance (in the stationary solver), the maximum outer iterations, and the maximum inner iterations per outer are $\tau_{\mathrm{opt}} = 1 \times 10^{-7}$, $\tau_{\mathrm{rel}} = 1 \times 10^{-3}$, $\mathrm{iter}_{\mathrm{out}}^{\max} = 100$, and $\mathrm{iter}_{\mathrm{in}}^{\max} = 3$, respectively. The equivalent relative permittivity curves are controlled to meet at the same point as depicted in Supplementary Fig. S1 by an additional volume fraction constraint $v_f = 50\%$. With a view to adjusting the objective near zero, a Heaviside filter is applied for the final material distribution in the design domain, with $\beta = 1000$ and $\eta = 0.4$. The optimised design and its rendered figures for this case are shown in Figs. 3**a-b** with the equivalent permittivity converged to $\varepsilon_{\mathrm{eff}} = 0.01 + 0.68\mathrm{i}$ at 300 MHz and $\varepsilon_{\mathrm{eff}} = -0.03 + 0.17\mathrm{i}$ at 1.2 GHz. Although the dopant material used in the designable zone takes different permittivity values in two modes (−531.52 in the 1st mode and −35.19 in the 2nd mode), the

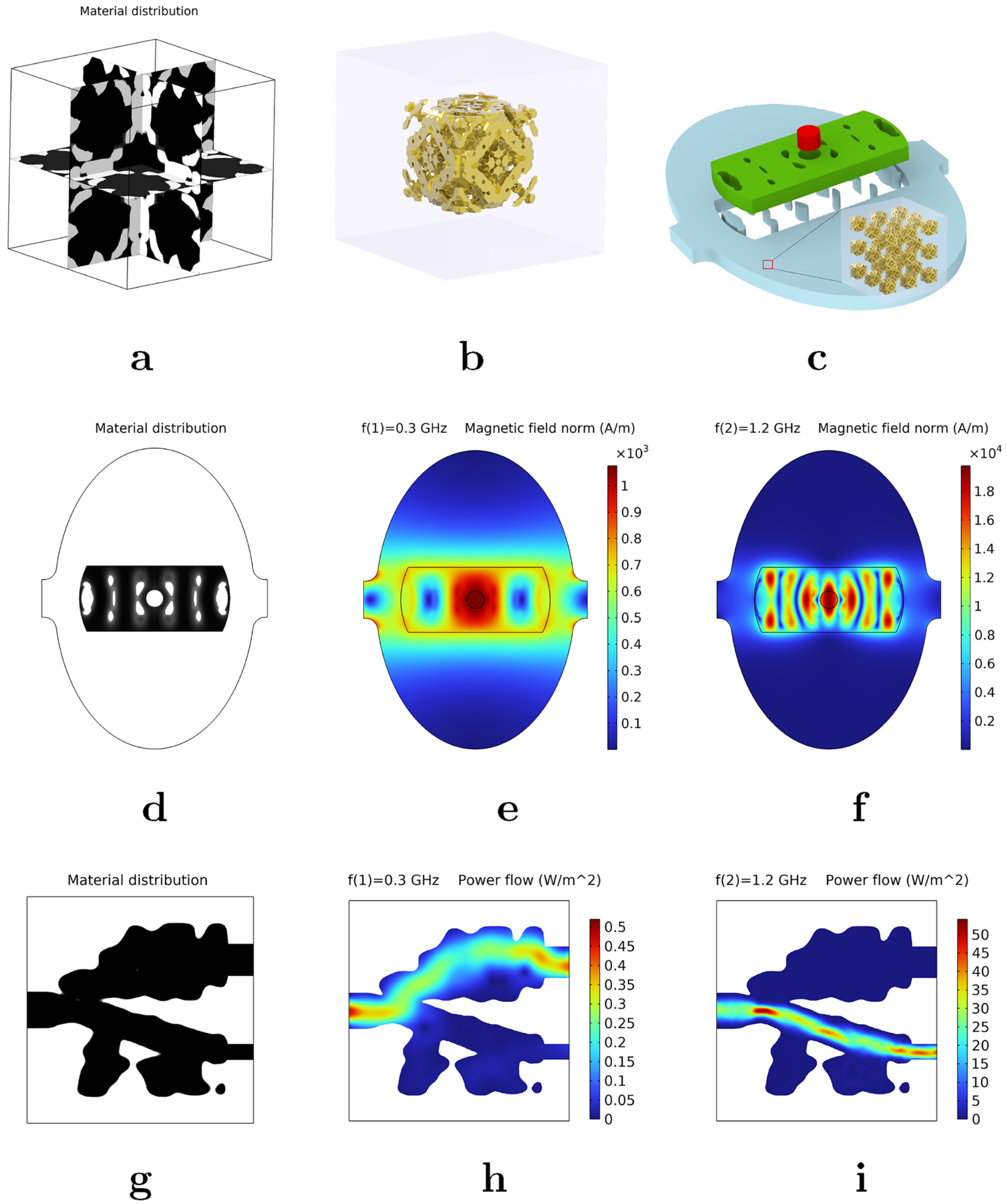

Fig. 3 The three topology optimisation steps. **a** Optimised density distribution inside the design domain of the ENZ unit cell. **b** Fully symmetric rendered unit design: the dopant (rendered in gold, made from copper calcium titanium oxide (CCTO) nanocomposites incorporated with 18 wt% multiwall carbon nanotube (MWCNT) [80]) is covered by polyethylene/XLPE dielectric. **c** An exploded view of the cavity resonator obtained from simulation reveals the metasurface. **d** Optimised material distribution in the cavity. **e** Magnetic field norm of the 1st mode. **f** Magnetic field norm of the 2nd mode. **g** Final topology design of the signal splitter. **h** Power flow at the 1st wavelength $\lambda_1 = 1$ m. **i** Power flow at the 2nd wavelength $\lambda_2 = 0.25$ m

optimiser can still compromise to guarantee the convergence of the objective function. This result can be used to create the "artificial" metamaterial for the host region of the cavity resonators, as shown in Fig. 3**c**.

3.2 High–κ cloak

An important goal of this work is to design a dielectric domain within the cavity that covers the sample. This "cloak" must have the ability to enhance the magnetic intensity in the sample space at resonance states corresponding to the input excitation signal. All the boundaries of the resonator are imposed by the perfectly electric conducting condition (PEC) $\hat{\mathbf{n}} \times \mathbf{E} = 0$, except for the two ports. For the purpose of eliminating intermediate design variables, an imaginary part is added to the material interpolation scheme as

$$\varepsilon_r(\rho) = \varepsilon_{\mathrm{ENZ}} + \rho(\varepsilon_r - \varepsilon_{\mathrm{ENZ}}) - \mathrm{i}\alpha\rho(1-\rho), \tag{8}$$

where α is a dependent scaling factor, and $\varepsilon_{\mathrm{ENZ}}$ and ε_r denote the relative permittivity of the materials used for the host and sample regions, respectively. The void phase of the design space is assumed to become ENZ medium when ρ becomes zero. In this circumstance, the local field enhancement task is achieved by maximising the square norm of the total magnetic field in the sample as

$$\begin{aligned} \max_{\rho(\mathbf{x})} \quad & \Phi = \sum_{j=1}^{\aleph_\lambda=2} \int_{\Omega_S} \|\mathbf{H}(\boldsymbol{\varepsilon}(\mathbf{x}))\|^2 \mathrm{d}\Omega_S, \\ \text{s.t.} \quad & \mathcal{L}_{EM}(\mathbf{E}(\mathbf{x}), \mathbf{H}(\mathbf{x}), \rho(\mathbf{x})) = f(\mathbf{x}), \\ & \varepsilon_{r,e}(\rho) = \varepsilon_{\mathrm{ENZ}} + \rho_e(\varepsilon_{r,c} - \varepsilon_{r,\mathrm{ENZ}}) - \mathrm{i}\alpha\rho(1-\rho_e), e = 1, 2, ..., \aleph_e, \\ & 0 \le \rho_e \le 1, e = 1, 2, ..., \aleph_D, \\ & \rho = 0 \forall \mathbf{x} \in \Omega \setminus \left\{\Omega_D, \Omega_S\right\}. \end{aligned} \tag{9}$$

The original cavity is designed in a 2.5D oval shape as shown in Fig. 2**b** with parameters $L = 120$ mm, $W = 90$ mm, $R_1 = 30$ mm, $w_1 = w_2 = 15$ mm, $w_3 = 26$ mm, $r_i = 3.5$ mm. There are two external ports that allow to receive and transmit radio frequency signals. For simplicity, the host region is implied as ENZ material with permittivity $\varepsilon_{\mathrm{ENZ}} = 0 + 0.1\mathrm{i}$. The liquid sample ($\varepsilon_i = 80$) is immersed inside the high-permittivity area in the centre of the cavity. The design domain is a curved rectangular dielectric medium made of strontium titanate ($SrTiO_3$, $\varepsilon_c = 310$). In this setting, the topology of the sample is fixed, and the designable density field is only valid in the green zone. The lumped port condition is used on the listener port with the characteristic impedance $Z_{\mathrm{ref}} = 50\,\Omega$. During the optimisation loop, a geometric constraint is added using a symmetric plane passing through the cavity's centroid and parallel to the two ports. In this instance, a mirror operation is applied to reflect the density field from the green zone to the dark blue one. Therefore, this strategy can ensure the symmetry of the resonator geometry, making this device more applicable for experiments. Our idea is to seek an optimal material distribution of the high–κ patch in a certain host variant. Subsequently, the invariant property and the performance indices will be verified and validated for other variants in the verification stage. The simulation is considered with the signal entering at the left port at two desired frequencies, 300 MHz and 1.2 GHz. In the meshing, the designable domain is discretised into 7968 mapped quadrilateral elements while the remaining area contains 13,387 free quadrilateral elements. Then the optimiser is called with the following parameters: $\tau_{\mathrm{opt}} = 1 \times 10^{-15}$, $\tau_{\mathrm{rel}} = 1 \times 10^{-3}$, $\mathrm{iter}_{\mathrm{out}}^{\max} = 200$, and $\mathrm{iter}_{\mathrm{in}}^{\max} = 10$, respectively. The numerical results for the oval variant are shown in Fig. 3**d**-**f** in which the sample region overlaps with the high B_1 as desired. Consequently, the peaks of the electric field are pushed out of the sample to prevent heating as shown in the Supplementary Fig. S4 and Fig. S5. In the higher mode, the effective B_1 field is more contracted than in the lower one, but its energy is dispersed in the high–κ cloak because of the shorter relative wavelength. The extruded design also ensures the uniformity of B_1 along the thickness direction, which is rather difficult to achieve with conventional inductors. The B_1 map in any circular slice will be discussed later in the verification step.

3.3 Demultiplexer

Demultiplexers are crucial components in modern optical communication systems, designed to separate and route different wavelengths of signals. These devices play a vital role in maximising the capacity and efficiency of optical networks by enabling the transmission of multiple channels over a single signal fibre. One of the key advantages of dielectric demultiplexers is their ability to operate across a wide range of wavelengths with high precision. They use carefully designed dielectric structures to achieve wavelength selectivity, which allows them to separate the incoming signal into distinct wavelength channels. This capability is especially important in wavelength-division multiplexing (WDM) systems, where multiple wavelengths of an electromagnetic wave are combined and transmitted together. Dielectric demultiplexers offer several advantages over other demultiplexing techniques. First, they provide low insertion loss, which means that most of the signal power is transmitted through the device without significant attenuation. This ensures efficient signal transmission and minimises signal degradation. Additionally, they offer excellent channel isolation, reducing crosstalk and interference between different wavelength channels. Christiansen and Sigmund [81] have efficiently introduced the inverse design task of this device for two optical wavelengths. In our work, the optimisation problem is set up for RF signals in a pure 2D mode with the assumption that the field behaviour does not change along the thickness. The goal is to find a structure that maximises the transmission performance from the combined source to the desired output for each frequency. On the left port, the incident plane wave $E_z = n_x \sin\left(0.5\pi(1 - 2\left|y - 10\right| / h_{\Gamma_1})\right)$ is imposed in the TE mode to describe the input signal. First-order scattering boundary conditions $\mathbf{n} \times (\nabla \times \mathbf{E}) = \mathrm{i}k\mathbf{n} \times (\mathbf{E} \times \mathbf{n})$ are also imposed on the remaining boundary of Ω. The constrained optimisation problem is then formulated as follows.

$$\begin{aligned}
\max_{\rho} \Phi &= \sum_{j=1}^{\aleph_\lambda=2} \frac{\int_{\Gamma_k} \langle \mathbf{P}(\lambda_j, \rho(\mathbf{x})) \rangle \mathrm{dx}}{\int_{\Gamma_1} \langle \mathbf{P}(\lambda_j, \rho(\mathbf{x})) \rangle \mathrm{dx}}, k \in \{2,3\}, \\
\text{s.t.} \quad \mathbf{f}(\lambda_j) &= \mathcal{L}_{EM}\left(\lambda_j, \varepsilon_r(\rho(\mathbf{x})), E_z\right)\mathbf{x}, \\
\varepsilon_{r,e}(\rho) &= 1 + \rho_e(\varepsilon_{r,c} - 1) - \mathrm{i}\alpha\rho(1 - \rho_e), \\
& \quad \mathrm{e} = 1, 2, ..., \aleph_e, \\
0 \le \rho_e &\le 1, e = 1, 2, ..., \aleph_D, \\
\rho &= 0 \forall \mathbf{x} \in \Omega \setminus \left\{\Omega_D, \Omega_S\right\}.
\end{aligned} \tag{10}$$

The problem description is shown in Fig. 2**c** with a square design domain $\Omega_D = \{(x, y) : 2.5 \le x \le 17.5, 2.5 \le y \le 17.5\}$ cm covered by air $\Omega = \{(x, y) : 0 \le x \le 20, 0 \le y \le 20\}$ cm as the background material where $\mathbf{k}_1$ and $\mathbf{k}_2$ are wave vectors in the double-resonant regime, $\Gamma_1 = \{(x, y) : x = 0, 8.6 \le y \le 11.4\}$ cm is the inlet which receives the combined signal from the resonator, $\Gamma_2 = \{(x, y) : x = 20, 13.6 \le y \le 16.4\}$ cm and $\Gamma_3 = \{(x, y) : x = 20, 4.3 \le y \le 5.7\}$ mm are boundaries of output waveguides. The in/out waveguides and the designable area (Ω_D) are made of the same material as the high–κ patch in the cavity ($\varepsilon_r = 310$). In the meshing, the designable domain is discretised into 5850 mapped quadrilateral elements while the waveguide port area contains 570 mapped quadrilateral elements. The surrounding air region is meshed with 4809 triangles. The set of optimisation parameters is chosen as: $\tau_{\mathrm{opt}} = 1 \times 10^{-3}$, $\tau_{\mathrm{rel}} = 1 \times 10^{-3}$, $\mathrm{iter}_{\mathrm{out}}^{\max} = 600$, and $\mathrm{iter}_{\mathrm{in}}^{\max} = 3$, respectively. After the simulation was run, the final design and the corresponding behaviour of the power flow at two desired frequencies (300 MHz and 1.2 GHz) are given in Fig. 3**g-i**, where the void area represents the background air medium. In this design, each guideline is connected to several electromagnetic Helmholtz resonators which are recognised easier in the higher frequency waveguide. In other words, the inverse design task in this problem is to find an appropriate combination of waveguides and resonators. The shape and size of the local resonators depend on the frequency couple as given in Supplementary Fig. S6 in which the lower frequency is raised to 500 MHz. It is observed that most of the power energy at two frequency levels is significantly decomposed and directed to the assigned ports, which can be assessed by effective transmission coefficients. The absolute transmittance T_{Abs} could be estimated as the total power flow through each output waveguide, while the relative transmittance T_{Rel} is the ratio of T_{Abs} to the input. They are listed in the Supplementary Table S1. The relative transmittance takes the value of 96% at 300 MHz and 85% at 1.2 GHz, while its maximum value achieved from the original approach in all settings is 86% [81]. Accordingly, the modified objective function based on relative transmittance is more advantageous than the one based on power flow in this RF range.

3.4 Numerical verification

In this subsection, the simulation is performed in the frequency domain to confirm the validity of the final designs obtained from the topology optimisation step. It is required to check if there are any changes in the eigenfrequencies of the original detector, because the effective density field shown in Fig. 3**d** contains a few intermediate density areas. Basically, the optimised high-dielectric patch acquired for the oval resonator will be reused to inspect the other designs. In particular, the eigenvalue problems have been solved for all cavity variants with the same high–κ sample cloak using the following equation:

$$\nabla \times \left(\frac{1}{\mu} \nabla \times \mathbf{E} \right) = \xi \varepsilon \mathbf{E}, \tag{11}$$

where $\xi = \omega^2$ is the eigenvalue. The electromagnetic arrangement is subsequently derived from a simulation result under an entry excitation at the observed eigenfrequencies. The magnetic field results of the first three variants in two eigenmodes, demonstrated in Fig. 4, show a similar distribution of the B_1 field and its direction over the circular slice of the sample in a double resonant configuration. B_1 field maps of the remaining candidates are provided in the Supplementary Fig. S7 and Fig. S8. Among the released geometries, the last six variants are more compatible with incorporation in commercial NMR systems than the first three, because their effective diameters are compatible with the bores in popular typical NMR magnets (55.9 mm for C-shaped and I-shaped, 40 mm for curved H-shaped, S-shaped, and D-shaped, 44.5 mm for finned-rect HSS) (Bruker's Ascend magnets offer two sizes of 54 mm standard-bore and 89 mm wide-bore in diameter, respectively). From this point of view, our resonators show the versatility of integration not only in standard NMR systems, but also for customised magnets, as their shapes could be modified to adapt to the system configuration.

It is necessary to investigate the B_1 field if the assumed flawless host is replaced by a unit cell structure as it reflects the practical working of the detectors. In the simulation procedure, only six host regions covered by the high–κ patch on its right side are filled with unit cells due to the limited physical memory of the computer (256 GB as described in Sect. 2.3). A detailed mapping scheme for simulation is described in the Supplementary Section 1 and Figs. S9–S11. The behaviour of the B_1 fields given in Fig. 5 is almost unchanged compared to Fig. 4**a** and Fig. 4**d**. From this point, we have achieved the dual-mode ENZ behaviour regardless of the frequency-dependent permittivity of the dopant as shown in the Supplementary Fig. S12. However, the intensity of the magnetic field in each eigenmode is slightly decreased due to the local concentration of the electric field

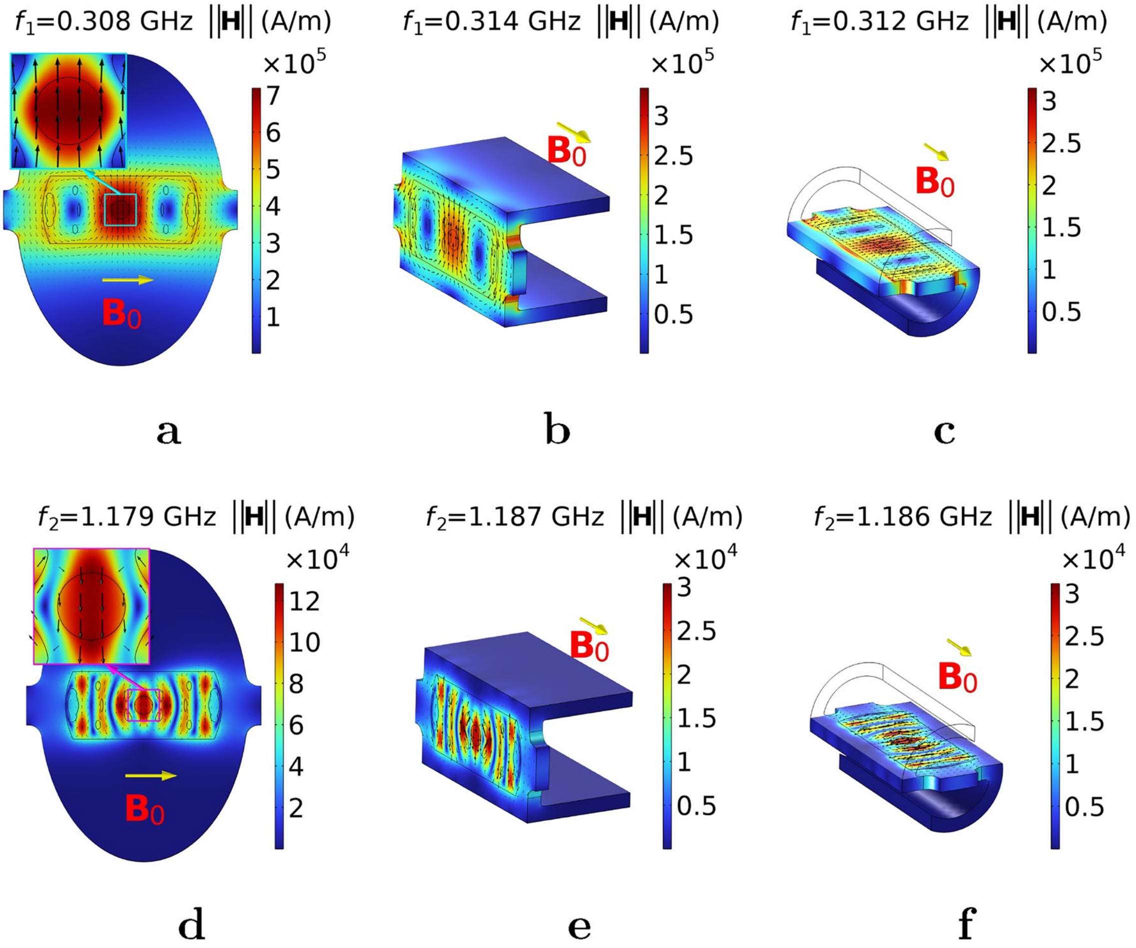

Fig. 4 B_1 field map inside three representative resonator geometry variants, in the double-resonant regime of operation. B_0 indicates the direction of the high static field in NMR spectroscopy. **a,d** B_1 field in two modes of the oval cavity, exposing its alignment and homogeneity in the sample. **b,e** B_1 field in two modes of the C-shaped cavity. **c,f** B_1 field in two modes of the S-shaped cavity

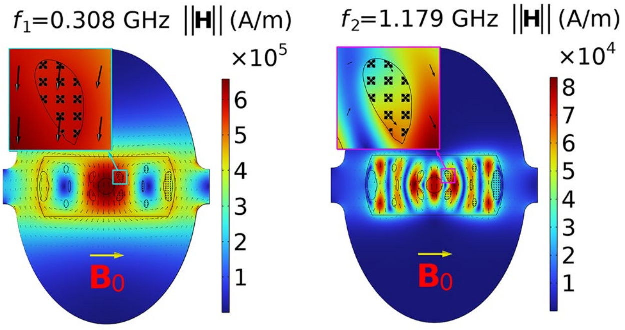

a 1st mode **b** 2nd mode

Fig. 5 The B_1 field maps in the double-resonant regime when some areas of the host region are replaced by the unit cell design. The field pattern is not significantly perturbed by this replacement, confirming equivalence of the discretisation. B_0 indicates the proper direction of the static magnetic field in NMR spectroscopy

in the unit cells, as depicted in the Supplementary Fig. S13. This implies that any practical unit cell design cannot dominate the theoretical ENZ medium in terms of performance.

More detailed views of the B_1 field in the sample region at two modes are shown in the Supplementary Fig. S14 and Fig. S15, in which the plots are scaled to individual global ranges set from 0 to the maximal magnetic intensity for each mode (7.75×10^5 A/m for mode 1, and 1.44×10^5 A/m for mode 2).

Excellent alignment of the B_1 field direction is achieved in all cases, but the highest field magnitude varies with the resonators. Although the field strength is lessened comparatively when the host shape is transformed from a planar 2.5D geometry to fully 3D shapes, the field homogeneity remains remarkably good. This is also quantitatively corroborated via the chart in Fig. 6**a**, which indicates that the B_1-uniformity values are around 98% in mode 1 and 95% in mode 2. The superiority of the cavity designs can be confirmed through the digital twin of the

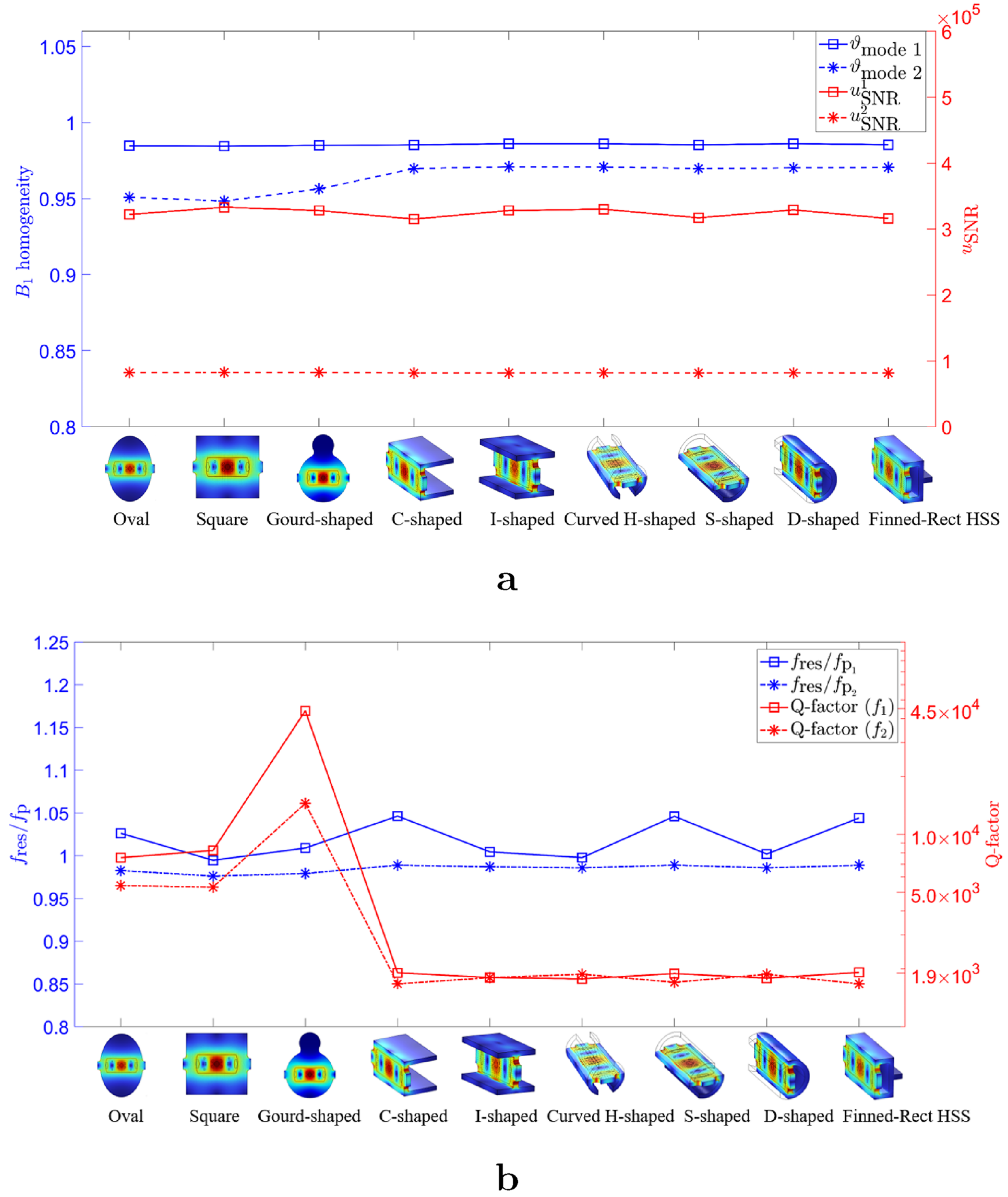

Fig. 6 **a** Uniformity of the B_1 field in the sample, and the detection sensitivities, for all candidate geometries. **b** Dependence of the normalised resonant frequencies and the Q-factors, on the deformation of the cavity shape

nutation signal, as given in the Supplementary Fig. S16. The decay rate of the nutation signal is determined by the RF field inhomogeneities, which are slightly worse in the second modes, as mentioned above. In these graphs, it is observed that cavity resonators require shorter pulse widths compared to conventional probes (normally > 10 μs). In addition, the sensitivity of the resonant cavity can be estimated as the quotient between the magnetic field intensity amplitude and the power loss density over the detector [82]

$$u_{\mathrm{SNR}} = \frac{\int\limits_{\Omega_S} \|\mathbf{H}\| \mathrm{d}\Omega}{\int\limits_{\Omega_S} \mathrm{d}\Omega \sqrt{\frac{1}{2} \int\limits_{\Omega} \sigma \|\mathbf{E}\|^2 \mathrm{d}\Omega}}, \tag{12}$$

where σ indicates the electrical conductivity field over the computational domain. The u_{SNR} curves in Fig. 6**a** show the stability of the sensitivity in double resonance as a function of the shape of the cavity.

From the above results, it is clear that despite their different geometry, the eigenfrequencies of these detectors vary by 4.77% (mode 1) and 2.38% (mode 2) from the plasma frequency. This statement is supported by the data of the diagram in Fig. 6**b**. Moreover, this diagram also shows a noticeable dependence of the Q-factor on the shape of cavities. The Q-factor is an important parameter that characterises resonance systems. It is determined as the ratio between the average energy stored and the dissipated power:

$$Q = \frac{\int\limits_{\Omega} (\varepsilon \mathbf{E} \cdot \mathbf{E}^* + \mu \mathbf{H} \cdot \mathbf{H}^*) \mathrm{d}\Omega}{\int\limits_{\Omega} \sigma \mathbf{E} \cdot \mathbf{E}^* \mathrm{d}\Omega}, \tag{13}$$

The average energy stored can be estimated by taking the volume integral of the energy density time average, and the dissipated power can be computed as resistive losses over the whole domain Ω. From this plot, the Q-factor takes the highest value for the gourd-shaped cavity and a similar value of around 1900 for 3D variants (in both modes).

In the next stage, an arbitrary variant is employed to explore the influences of the sample's permittivity on the resonant frequencies and the Q-factors. In this case, the D-shaped candidate was randomly chosen as a test object for investigation. Although the permittivity of the sample varied in a range of 2 to 80 in the test, other parameters remained without any modification.

The diagram in Fig. 7 illustrates the dependence of the resonant frequency and the Q-factor on the sample's permittivity. In fact, the eigenfrequencies and the first Q-factor are almost unchanged, whereas the Q-factor of the 2nd mode increases linearly by about 9.6% over the entire permittivity range. This reveals another interesting invariant property of the resonator and proves the independence of the device from the solvent type present in the sample space.

One of the last important specifications is the set of scattering parameters representing the behaviour of the device under external excitation. S-parameters can be retrieved using the electric field, obtained from the simulation as follows.

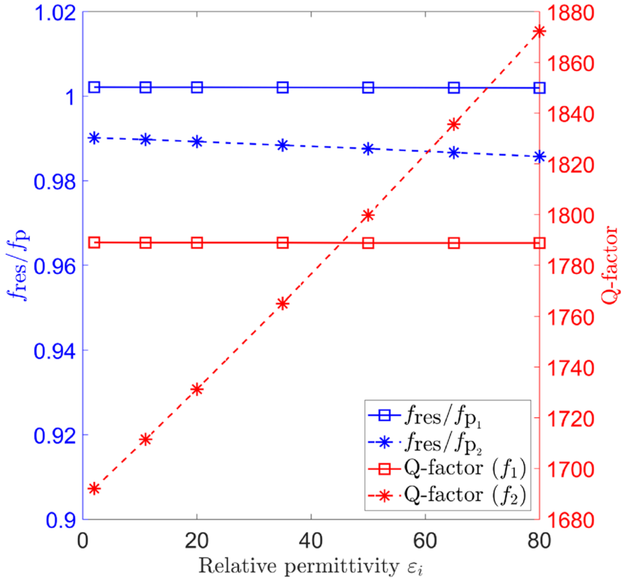

Fig. 7 Dependence of the normalised resonance frequencies and the resonator Q-factors on a sample's dielectric constant

$$\begin{aligned} S_{11} &= \frac{\int\limits_{\Gamma_1} \left(\mathbf{E} - \mathbf{E}_0\right) \cdot \mathbf{E}_0^* \mathrm{d}\Gamma}{\int\limits_{\Gamma_1} \mathbf{E}_0 \cdot \mathbf{E}_0^* \mathrm{d}\Gamma}, \\ S_{21} &= \frac{\int\limits_{\Gamma_2} \mathbf{E} \cdot \mathbf{E}_0^* \mathrm{d}\Gamma}{\int\limits_{\Gamma_1} \mathbf{E}_0 \cdot \mathbf{E}_0^* \mathrm{d}\Gamma}, \end{aligned} \tag{14}$$

where $\bullet^*$ denotes the complex conjugate. The S-parameters of all candidates are given in Fig. 8. S_{11} results take very small negative values, which implies that there are no reflections at the inlet ports for all cavities. This is absolutely suitable with the high Q-factors obtained above. The positive S_{21} indicates that the transmitted signal is amplified at the outlet ports, as expected from a high-Q resonator. In the majority of scenarios examined, the first frequency f_1 component arriving from the second port, captured by S_{21}, remains constant, indicating a high level of stability. In contrast, f_2 undergoes significant changes as it outperforms f_1 in planar resonator situations, but eventually experiences a decrease, leading to lower values for most fully 3D geometries. Furthermore, the narrow S-parameter spectra implement a strong frequency selection, which is consistent with the results regarding the sensitivity and Q-factor presented in Fig. 6.

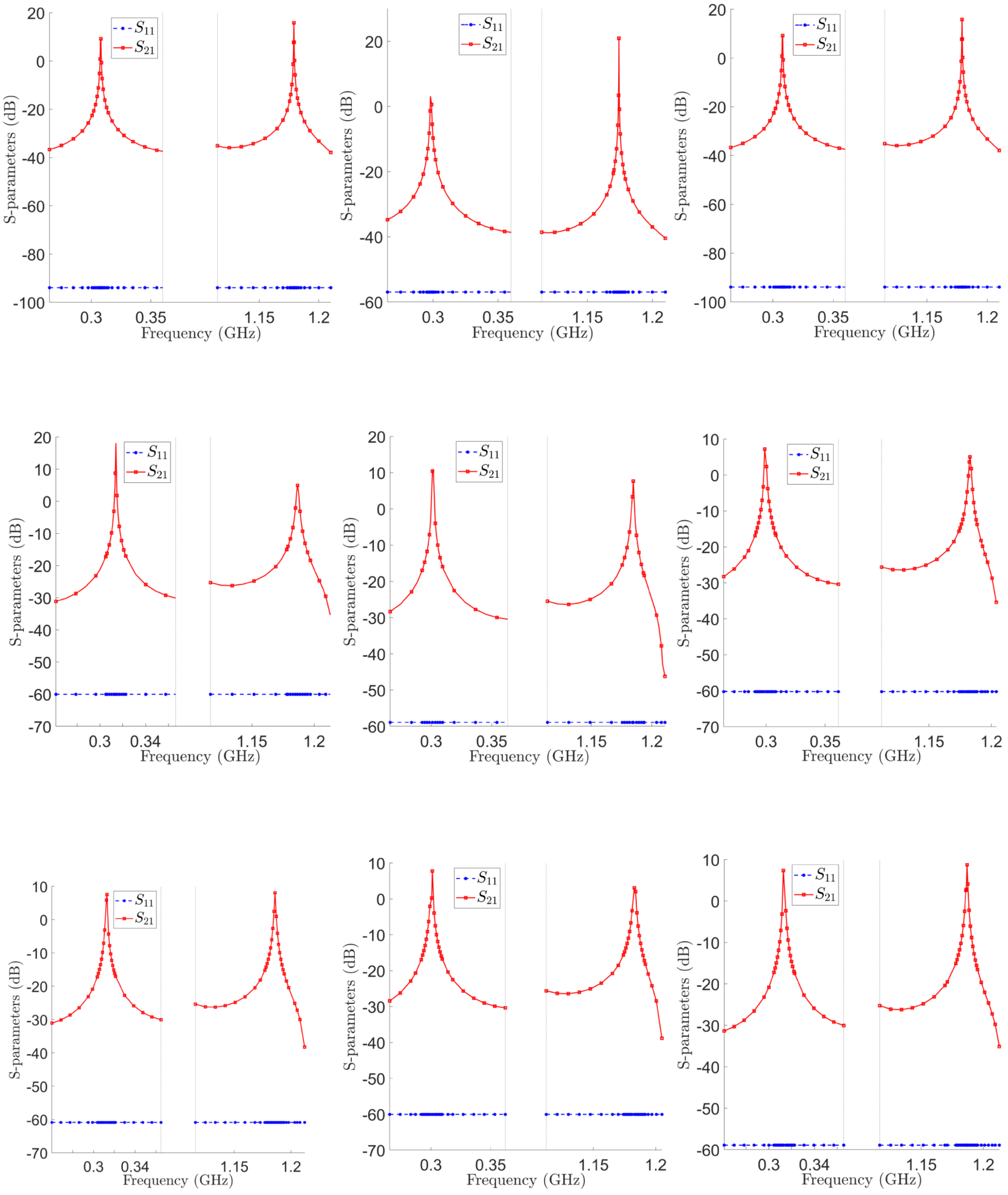

Fig. 8 **a–i** S-parameter estimation for all cavity variants

4 Conclusion

Ultra-high field nuclear magnetic resonance (UHF-NMR) offers significant advantages over lower field strengths. It enables the study of samples with lower concentrations with improved sensitivity, better resolution, and high spectral dispersion. As a result, it is especially valuable for investigating complex macromolecules, dynamic processes, weak interactions, paramagnetic systems, and solid-state materials. These capabilities are certainly applicable in numerous fields, such as proteomics, metabolomics, biomarker identification, and materials science, making UHF-NMR a powerful and indispensable tool for many in-depth research tasks.

We have demonstrated a new concept for double-resonant NMR detection that employs optimised frequency-invariant cavity resonators to overcome some shortcomings that remain in frequency-scaled LC resonators. By surrounding the cavity with an ENZ medium, the resonant frequencies of the metamaterial-embedded detector are controlled by a permittivity's contribution to dispersion, instead of its geometrical transformation. In other words, the cavity topology primarily influences the B_1 field intensity and the Q-factor, rather than its natural frequency. Especially, it is shown numerically that such a detector could be applied to a wide variety of different liquid samples at the locked-in frequencies, without re-tuning the resonator, while its Q-factor is only slightly perturbed. The proposed approach contributes a paradigm shift to the field of high-sensitivity probe design for NMR applications. The core novelty of our methodology lies in its generality, as it is suitable for application to all cavity-based resonators. Based on the inverse design principle, we provide a flexible and innovative framework that overcomes the barrier of the lumped circuit approach. Furthermore, we highlight the potential of our approach to serve as a reference point for other NMR experts facing challenges in multiresonant UHF probe design within their specialised research fields. The applicability of this method makes it a powerful tool for a new generation of Larmor frequency-preserving detectors, independent of any external perturbation that might be imposed by a specific MR measurement. The insensitivity to resonator geometry opens an evolution pathway in which customisable and deformable resonant devices can be applied in NMR spectroscopy and other electromagnetic applications with a similar design language. Additionally, it is emphasised that innovative zero-index metamaterials can be developed to operate in the RF dual-mode through optimisation algorithms. This achievement inspires novel design viewpoints in which unique electromagnetic responses are able to activate in broadband devices. While our material design has been focused on enhancing the sensitivity and performance of NMR detectors, we believe that further potential applications could be explored in antenna technology, cloaking devices, wireless communication, and signal processing.

5 Supplementary information

This article has an accompanying supplementary material.

Supplementary Information The online version contains supplementary material available at https://doi.org/10.1007/s00366-024-02068-x.

Acknowledgements The authors are supported by the DFG, Germany (OptiMuM, 446995632). J.G.K. acknowledges support from the ERC-SyG (HiSCORE, 951459). V.B. and J.G.K. thank the Deutsche Forschungsgemeinschaft for funding via the SFB 1527 HyPERiON. The authors acknowledge the support of the Helmholtz Society through the program Materials Systems Engineering, and the Karlsruhe Institute of Technology for operating a safe research environment.

Author Contributions J.G.K. conceived of the original idea; K.C. designed the optimisation problems and implemented all simulations; all authors analysed the results; J.G.K. acquired funding for this research; V.B. and J.G.K. provided supervision; all authors reviewed the manuscript.

Funding Open Access funding enabled and organized by Projekt DEAL.

Data Availability The data generated in this paper are freely available upon reasonable request.

Declarations

Conflict of interest The authors have no conflict of interest to declare.

Open Access This article is licensed under a Creative Commons Attribution 4.0 International License, which permits use, sharing, adaptation, distribution and reproduction in any medium or format, as long as you give appropriate credit to the original author(s) and the source, provide a link to the Creative Commons licence, and indicate if changes were made. The images or other third party material in this article are included in the article's Creative Commons licence, unless indicated otherwise in a credit line to the material. If material is not included in the article's Creative Commons licence and your intended use is not permitted by statutory regulation or exceeds the permitted use, you will need to obtain permission directly from the copyright holder. To view a copy of this licence, visit http://creativecommons.org/licenses/by/4.0/.

References

1. Hoult D (2011) The principle of reciprocity. J Mag Resonance 213(2):344–346
2. Lufkin R, Votruba J, Reicher M, Bassett L, Smith SD, Hanafee W (1986) Solenoid surface coils in magnetic resonance imaging. Am J Roentgenol 146(2):409–412
3. Syms R, Ahmad M, Young I, Li Y, Hand J, Gilderdale D (2005) MEMS Helmholtz coils for magnetic resonance imaging. J Micromech Microeng 15(7):1
4. Stringer JA, Bronnimann CE, Mullen CG, Zhou DH, Stellfox SA, Li Y, Williams EH, Rienstra CM (2005) Reduction of RF-induced sample heating with a scroll coil resonator structure for solid-state NMR probes. J Mag Resonance 173(1):40–48
5. Dohi T, Kuwana K, Matsumoto K, Shimoyama I (2007). A standing micro coil for a high resolution MRI. In: TRANSDUCERS 2007 - 2007 International Solid-State Sensors, Actuators and Microsystems Conference, 1313–1316
6. Tang F, Hao J, Freschi F, Niu C, Repetto M, Liu F, Crozier S (2019) A cone-shaped gradient coil design for high-resolution MRI head imaging. Phys Med Biol 64(8):085003
7. Leidich S, Braun M, Gessner T, Riemer T (2009) Silicon cylinder spiral coil for nuclear magnetic resonance spectroscopy of nanoliter samples. Concepts Mag Resonance Part B 35(1):11–22
8. Takahashi H, Dohi T, Matsumoto K, Shimoyama I (2007). A micro planar coil for local high resolution magnetic resonance imaging. In: 2007 IEEE 20th International Conference on Micro Electro Mechanical Systems (MEMS), 549–552 . IEEE
9. Shen G.X, Boada F.E, Thulborn K.R (1997). Dual-frequency, dual-quadrature, birdcage RF coil design with identical B1 pattern for sodium and proton imaging of the human brain at 1.5 T. Magnetic Resonance in Medicine 38(5), 717–725
10. Webb A (2014) Cavity-and waveguide-resonators in electron paramagnetic resonance, nuclear magnetic resonance, and magnetic resonance imaging. Progress in Nuclear Magnetic Resonance Spectroscopy 83:1–20

11. Aydé R, Gaborit G, Dahdah J, Duvillaret L, Courjal N, Guyot C, Sablong R, Perrier A-L, Beuf O (2014) Unbiased electro-optic waveguide as a sensitive nuclear magnetic resonance sensor. IEEE Photonics Technology Letters 26(12):1266–1269
12. Van Bentum P, Janssen J, Kentgens A, Bart J, Gardeniers JG (2007) Stripline probes for nuclear magnetic resonance. Journal of Magnetic Resonance 189(1):104–113
13. Hernandez D, Kim K-N (2020) A review on the RF coil designs and trends for ultra high field magnetic resonance imaging. Investigative Magnetic Resonance Imaging 24(3):95–122
14. Zalesskiy SS, Danieli E, Blumich B, Ananikov VP (2014) Miniaturization of NMR systems: Desktop spectrometers, microcoil spectroscopy, and NMR on a chip for chemistry, biochemistry, and industry. Chemical Reviews 114(11):5641–5694
15. Gruber B, Stockmann JP, Mareyam A, Keil B, Bilgic B, Chang Y, Kazemivalipour E, Beckett AJS, Vu AT, Feinberg DA, Wald LL (2023) A 128-channel receive array for cortical brain imaging at 7T. Magnetic Resonance in Medicine 90(6):2592–2607
16. Qu H, Wang W, Wu H, Wang C, Wang Y, Wang Q, Liu F (2024). Superconducting shim coils design for the 9.4 tesla whole-body mri magnet. IEEE Transactions on Applied Superconductivity **34**(2)
17. Purcell EM, Torrey HC, Pound RV (1946) Resonance absorption by nuclear magnetic moments in a solid. Physical Review 69(1–2):37
18. Niessen HG, Trautner P, Wiemann S, Bargon J, Woelk K (2002) The toroid cavity autoclave for high-pressure and variable-temperature in situ nuclear magnetic resonance studies. Review of Scientific Instruments 73(3):1259–1266
19. Colton J.S, Wienkes L (2009). Resonant microwave cavity for 8.5–12 GHz optically detected electron spin resonance with simultaneous nuclear magnetic resonance. Review of Scientific Instruments 80(3), 035106
20. Enoch S, Tayeb G, Sabouroux P, Guérin N, Vincent P (2002) A metamaterial for directive emission. Physical Review Letters 89(21):213902
21. Garcia N, Ponizovskaya E, Xiao JQ (2002) Zero permittivity materials: Band gaps at the visible. Applied Physics Letters 80(7):1120–1122
22. Ziolkowski RW (2004) Propagation in and scattering from a matched metamaterial having a zero index of refraction. Physical Review E 70(4):046608
23. Silveirinha M, Engheta N (2006) Tunneling of electromagnetic energy through subwavelength channels and bends using ε-near-zero materials. Physical Review Letters 97(15):157403
24. Silveirinha MG, Engheta N (2007) Theory of supercoupling, squeezing wave energy, and field confinement in narrow channels and tight bends using ε near-zero metamaterials. Physical Review B 76(24):245109
25. Campione S, Wendt JR, Keeler GA, Luk TS (2016) Near-infrared strong coupling between metamaterials and epsilon-near-zero modes in degenerately doped semiconductor nanolayers. ACS Photonics 3(2):293–297
26. Liberal I, Engheta N (2016) Nonradiating and radiating modes excited by quantum emitters in open epsilon-near-zero cavities. Science Advances 2(10):1600987
27. Kim J, Dutta A, Naik GV, Giles AJ, Bezares FJ, Ellis CT, Tischler JG, Mahmoud AM, Caglayan H, Glembocki OJ et al (2016) Role of epsilon-near-zero substrates in the optical response of plasmonic antennas. Optica 3(3):339–346
28. Adams DC, Inampudi S, Ribaudo T, Slocum D, Vangala S, Kuhta NA, Goodhue WD, Podolskiy VA, Wasserman D (2011) Funneling Light through a Subwavelength Aperture with Epsilon-Near-Zero Materials. Physical Review Letters 107:133901
29. Lovat G, Burghignoli P, Capolino F, Jackson DR, Wilton DR (2006) Analysis of directive radiation from a line source in a metamaterial slab with low permittivity. IEEE Transactions on Antennas and Propagation 54(3):1017–1030
30. Powell DA, Alù A, Edwards B, Vakil A, Kivshar YS, Engheta N (2009) Nonlinear control of tunneling through an epsilon-near-zero channel. Physical Review B 79(24):245135
31. Suchowski H, O'Brien K, Wong ZJ, Salandrino A, Yin X, Zhang X (2013) Phase mismatch-free nonlinear propagation in optical zero-index materials. Science 342(6163):1223–1226
32. Kinsey N, DeVault C, Kim J, Ferrera M, Shalaev V, Boltasseva A (2015) Epsilon-near-zero Al-doped ZnO for ultrafast switching at telecom wavelengths. Optica 2(7):616–622
33. Alam MZ, De Leon I, Boyd RW (2016) Large optical nonlinearity of indium tin oxide in its epsilon-near-zero region. Science 352(6287):795–797
34. Li C, Tian X, Yang G, Dev SU, Allen MS, Allen JW, Harutyunyan H (2023) Invertible optical nonlinearity in epsilon-near-zero materials. Physical Review Research 5:013198
35. Wu H, Zhang Z, Wang C, Abualnaja KM, Abo-Dief HM, Hou Q, Algadi H, Yin R, Liu X, Xie P et al (2023) Radio-frequency broadband epsilon-near-zero response in biocompatible silver nanoparticles/polystyrene films with three-dimensional honeycomb-like superstructures. Advanced Composites and Hybrid Materials 6(6):206
36. Qu Y, Zhou Y, Manshaii F, Wang K, Deng C, Liu Y (2024) Three-dimensional random network of metacomposites by synergizing multi-walled carbon nanotube-carbon black for tunable epsilon-negative and epsilon-near-zero responses. Composites Part A: Applied Science and Manufacturing 186:108410
37. Liberal I, Mahmoud AM, Engheta N (2016) Geometry-invariant resonant cavities. Nature Communications 7(1):1–7
38. Bendsøe MP, Kikuchi N (1988) Generating optimal topologies in structural design using a homogenization method. Computer Methods in Applied Mechanics and Engineering 71(2):197–224
39. Bendsoe MP, Sigmund O (2003) Topology Optimization: Theory, Methods, and Applications. Springer, New York
40. Andreasen CS, Sigmund O (2013) Topology optimization of fluid-structure-interaction problems in poroelasticity. Computer Methods in Applied Mechanics and Engineering 258:55–62
41. Christiansen RE, Fernandez-Grande E (2016) Design of passive directional acoustic devices using Topology Optimization-from method to experimental validation. The Journal of the Acoustical Society of America 140(5):3862–3873
42. Alexandersen J, Andreasen CS (2020) A review of topology optimisation for fluid-based problems. Fluids 5(1):29
43. Byun J.-k, Park I.-h, Hahn S.-y (2002). Topology optimization of electrostatic actuator using design sensitivity. IEEE Transactions on Magnetics 38(2), 1053–1056
44. Jensen JS, Sigmund O (2011) Topology optimization for nanophotonics. Laser & Photonics Reviews 5(2):308–321
45. Zhang J, Ning L, Hao Y, Sang T (2021) Topology optimization for crashworthiness and structural design of a battery electric vehicle. International Journal of Crashworthiness 26(6):651–660
46. Hidaka Y, Sasaki H (2021) Topology optimization of electrical devices using Gaussian filter. Journal of Advanced Simulation in Science and Engineering 8(1):98–113
47. Zhou S, Li W, Li Q (2010) Level-set based topology optimization for electromagnetic dipole antenna design. Journal of Computational Physics 229(19):6915–6930
48. Hassan E, Wadbro E, Berggren M (2014) Topology optimization of metallic antennas. IEEE Transactions on Antennas and Propagation 62(5):2488–2500
49. Jensen JS, Sigmund O (2004) Systematic design of photonic crystal structures using topology optimization: Low-loss waveguide bends. Applied Physics Letters 84(12):2022–2024
50. Wang F, Jensen JS, Sigmund O (2011) Robust topology optimization of photonic crystal waveguides with tailored

dispersion properties. Journal of the Optical Society of America B 28(3):387–397

51. Gao J, Xue H, Gao L, Luo Z (2019) Topology optimization for auxetic metamaterials based on isogeometric analysis. Computer Methods in Applied Mechanics and Engineering 352:211–236
52. Zhang H, Luo Y, Kang Z (2018) Bi-material microstructural design of chiral auxetic metamaterials using topology optimization. Composite Structures 195:232–248
53. Diaz AR, Sigmund O (2010) A topology optimization method for design of negative permeability metamaterials. Structural and Multidisciplinary Optimization 41:163–177
54. Dong H-W, Zhao S-D, Wang Y-S, Zhang C (2017) Topology optimization of anisotropic broadband double-negative elastic metamaterials. Journal of the Mechanics and Physics of Solids 105:54–80
55. Othmer C, De Villiers E, Weller H (2007). Implementation of a continuous adjoint for topology optimization of ducted flows. In: 18th AIAA Computational Fluid Dynamics Conference, p. 3947
56. Oktay E, Akay H, Merttopcuoglu O (2011) Parallelized structural topology optimization and CFD coupling for design of aircraft wing structures. Computers & Fluids 49(1):141–145
57. Koga AA, Lopes ECC, Nova HFV, De Lima CR, Silva ECN (2013) Development of heat sink device by using topology optimization. International Journal of Heat and Mass Transfer 64:759–772
58. Byun J-K, Park I-H (2007) Design of dielectric waveguide filters using topology optimization technique. IEEE Transactions on Magnetics 43(4):1573–1576
59. Yamasaki S, Nomura T, Sato K, Michishita N, Yamada Y, Kawamoto A (2012) Level set-based topology optimization targeting dielectric resonator-based composite right-and left-handed transmission lines. International Journal for Numerical Methods in Engineering 89(10):1272–1295
60. Deng Y, Liu Z, Liu Y, Wu Y (2017) Inverse design of dielectric resonator cloaking based on topology optimization. Plasmonics 12:1717–1723
61. Albrechtsen M, Vosoughi Lahijani B, Christiansen R.E, Nguyen V.T.H, Casses L.N, Hansen S.E, Stenger N, Sigmund O, Jansen H, Mørk J, et al (2022). Nanometer-scale photon confinement in topology-optimized dielectric cavities. Nature Communications 13(1), 6281
62. Deng Y, Liu Z, Song C, Wu J, Liu Y, Wu Y (2015) Topology optimization-based computational design methodology for surface plasmon polaritons. Plasmonics 10:569–583
63. Deng Y, Liu Z, Song C, Hao P, Wu Y, Liu Y, Korvink JG (2016) Topology optimization of metal nanostructures for localized surface plasmon resonances. Structural and Multidisciplinary Optimization 53:967–972
64. Andkjær J, Sigmund O (2011) Topology optimized low-contrast all-dielectric optical cloak. Applied Physics Letters 98(2):021112
65. Nomura T, Sato K, Taguchi K, Kashiwa T, Nishiwaki S (2007) Structural topology optimization for the design of broadband dielectric resonator antennas using the finite difference time domain technique. International Journal for Numerical Methods in Engineering 71(11):1261–1296
66. Economou E (1969) Surface plasmons in thin films. Physical Review 182(2):539
67. Pitarke J, Silkin V, Chulkov E, Echenique P (2006) Theory of surface plasmons and surface-plasmon polaritons. Reports on Progress in Physics 70(1):1
68. Kawata S (2001) Near-field Optics and Surface Plasmon Polaritons, vol 81. Springer, Heidelberg
69. Ditlbacher H, Krenn JR, Schider G, Leitner A, Aussenegg FR (2002) Two-dimensional optics with surface plasmon polaritons. Applied Physics Letters 81(10):1762–1764
70. Zayats AV, Smolyaninov II, Maradudin AA (2005) Nano-optics of surface plasmon polaritons. Physics Reports 408(3–4):131–314
71. Melikyan A, Alloatti L, Muslija A, Hillerkuss D, Schindler PC, Li J, Palmer R, Korn D, Muehlbrandt S, Van Thourhout D et al (2014) High-speed plasmonic phase modulators. Nature Photonics 8(3):229–233
72. Unal G, Aksun M (2015) Bridging the gap between RF and optical patch antenna analysis via the cavity model. Scientific Reports 5(1):15941
73. Salamin Y, Heni W, Haffner C, Fedoryshyn Y, Hoessbacher C, Bonjour R, Zahner M, Hillerkuss D, Leuchtmann P, Elder DL et al (2015) Direct conversion of free space millimeter waves to optical domain by plasmonic modulator antenna. Nano Letters 15(12):8342–8346
74. Zhang HC, Liu S, Shen X, Chen LH, Li L, Cui TJ (2015) Broadband amplification of spoof surface plasmon polaritons at microwave frequencies. Laser & Photonics Reviews 9(1):83–90
75. Guan D-F, You P, Zhang Q, Lu Z-H, Yong S-W, Xiao K (2017) A wide-angle and circularly polarized beam-scanning antenna based on microstrip spoof surface plasmon polariton transmission line. IEEE Antennas and Wireless Propagation Letters 16:2538–2541
76. Gao X, Zhou L, Cui TJ (2015) Odd-mode surface plasmon polaritons supported by complementary plasmonic metamaterial. Scientific Reports 5(1):9250
77. Monk P (2003) Finite Element Methods for Maxwell's Equations. Oxford University Press, Oxford
78. Duff IS, Koster J (1999) The design and use of algorithms for permuting large entries to the diagonal of sparse matrices. SIAM Journal on Matrix Analysis and Applications 20(4):889–901
79. Svanberg K (2002) A class of globally convergent optimization methods based on conservative convex separable approximations. SIAM Journal on Optimization 12(2):555–573
80. Cheng C, Wu Y, Qu Y, Ma R, Fan R (2020) Radio-frequency negative permittivity of carbon nanotube/copper calcium titanate ceramic nanocomposites fabricated by spark plasma sintering. Ceramics International 46(2):2261–2267
81. Christiansen RE, Sigmund O (2021) Inverse design in photonics by topology optimization: tutorial. Journal of the Optical Society of America B 38(2):496–509
82. Moussu MA, Abdeddaim R, Dubois M, Georget E, Webb AG, Nenasheva E, Belov P, Glybovski S, Ciobanu L, Enoch S (2020) A semi-analytical model of high-permittivity dielectric ring resonators for magnetic resonance imaging. IEEE Transactions on Antennas and Propagation 68(8):6317–6329

Publisher's Note Springer Nature remains neutral with regard to jurisdictional claims in published maps and institutional affiliations.